AGU Publications

Journal of Advances in Modeling Earth Systems

Supporting information for

A tool for generating fast *k*-distribution gas-optics models for weather and climate applications

Robin J. Hogan[1] **and Marco Matricardi**[1]

[1]European Centre for Medium-Range Weather Forecasts, Reading, UK

Contents of this file

Figures S1 to S10.

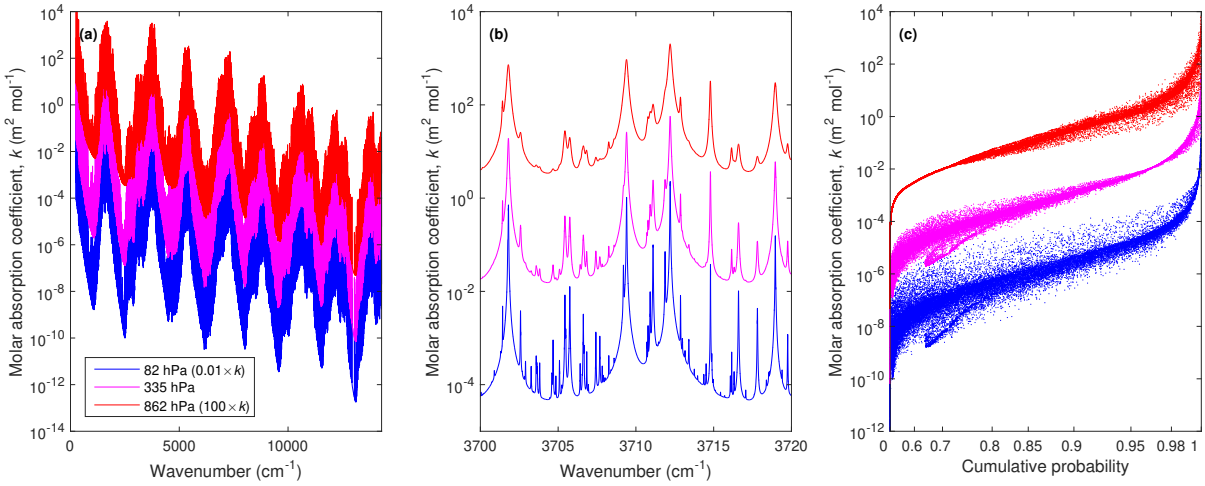

Figure S1: (a) H_2O molar absorption coefficient at three pressures for the CKDMIP 'median' standard atmosphere, in the near-infrared part of the shortwave spectrum; (b) the same but zooming in on a narrow spectral interval; (c) the corresponding cumulative probability where reordering has been performed according to the approximate height of peak solar heating rate. The 'pinch points' in panel c highlight that, despite imperfect correlation of the spectra between levels (due primarily to pressure broadening apparent in panel b), the reordering has been done in such a way that at a particular height (or pressure), the absorption coefficients are most accurately reordered for the wavenumbers that contribute most to the solar heating at that height. Note that in all three panels the absorption coefficients of the highest and lowest pressures have been multiplied or divided by 100 to aid visualization of the data (see legend in panel a).

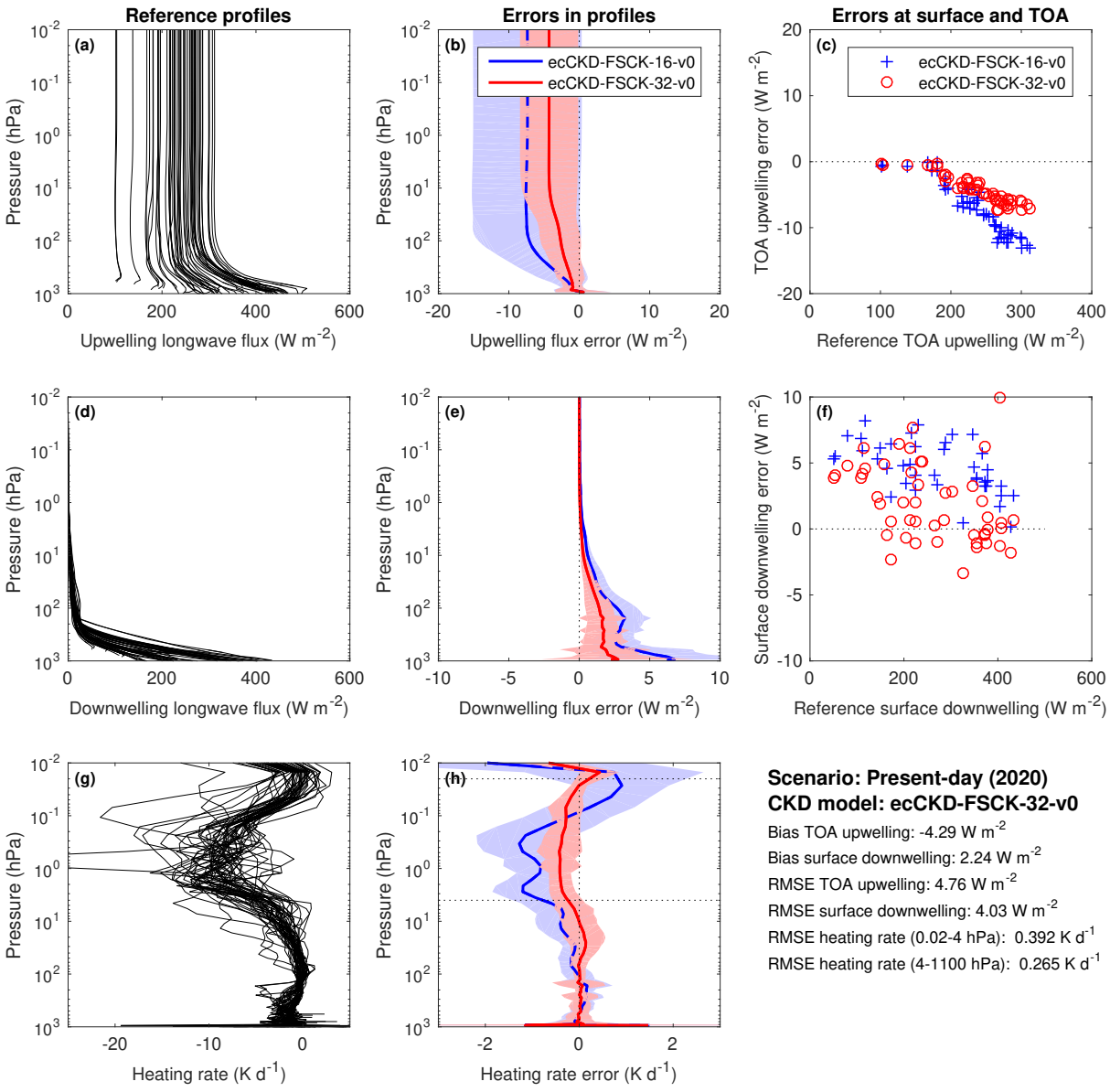

Figure S2: As Fig. 5 except that the evaluation was performed using v0 of the longwave look-up tables (i.e. without the optimization step) rather than the final version. Thus the difference from Fig. 5 demonstrates the importance of the optimization. Note the different scales in some of the panels compared to Fig. 5.

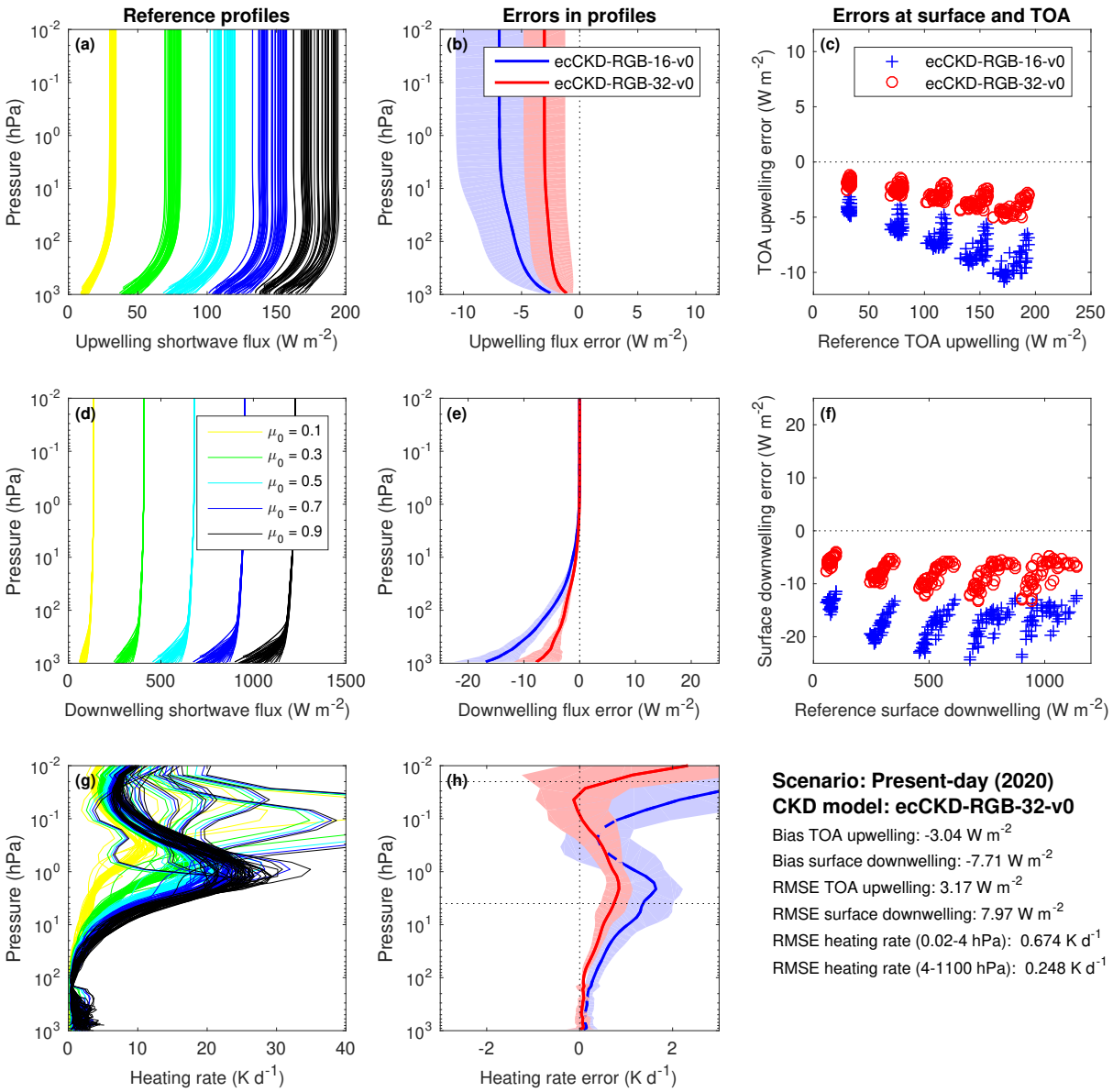

Figure S3: As Fig. 7 except that the evaluation was performed using v0 of the shortwave look-up tables (i.e. without the optimization and scaling steps). Note the different scales in some of the panels compared to Fig. 7.

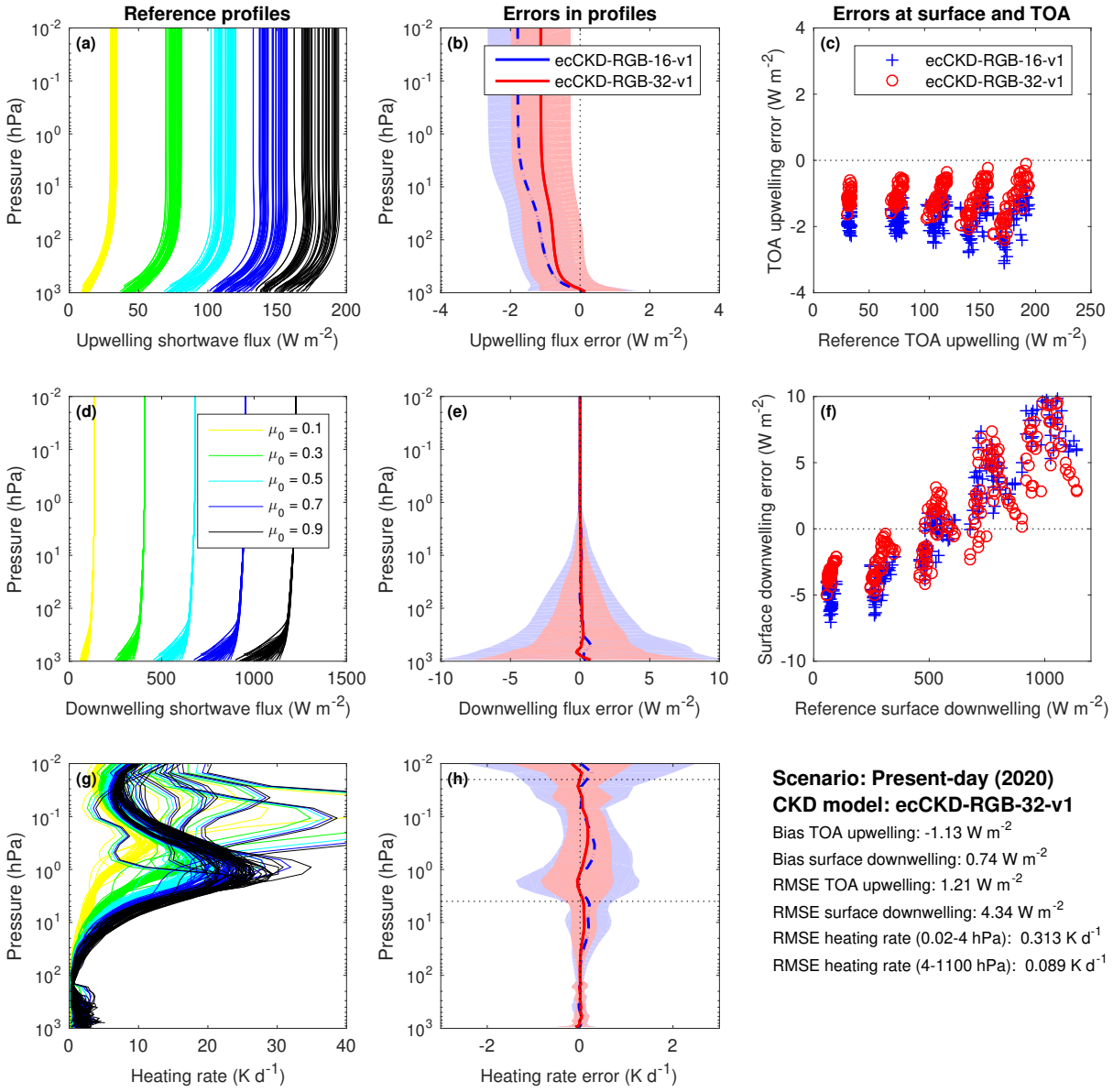

Figure S4: As Figs. 7 and S3 except that the evaluation was performed using v1 of the shortwave look-up tables (i.e. after the scaling step but before the optimization step). Thus the difference from Fig. S3 demonstrates the value of the scaling step especially to remove the bias in downwelling fluxes, while the difference from Fig. 7 demonstrates value of the optimization step to reduce both bias and scatter. Note the different scales in some of the panels compared to Fig. 7.

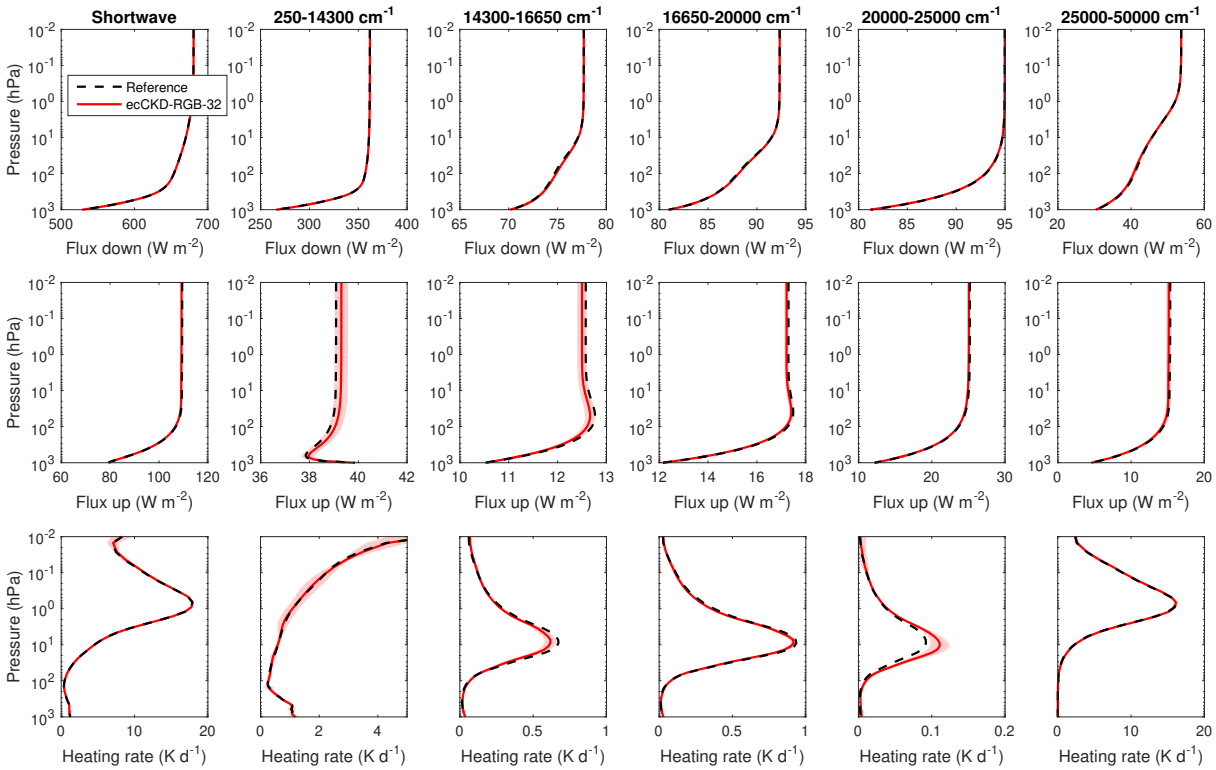

Figure S5: Supporting information for Fig. 7: comparison of profiles of mean fluxes and heating rates between line-by-line calculations on the 50 independent present-day 'Evaluation-2' CKDMIP profiles, and equivalent values computed using the ecCKD 32-term RGB model, averaged over five solar zenith angles. The leftmost column shows broadband values and the remaining five columns show values in each of the five RGB bands: (from left to right) near-infrared, red, green, blue and ultraviolet. The generally good agreement suggests that the accuracy of individual bands is not compromised by the weighting of the broadband fluxes and heating rates in the optimization. As in Fig. 7, the shaded regions encompass 95% of the errors in individual profiles.

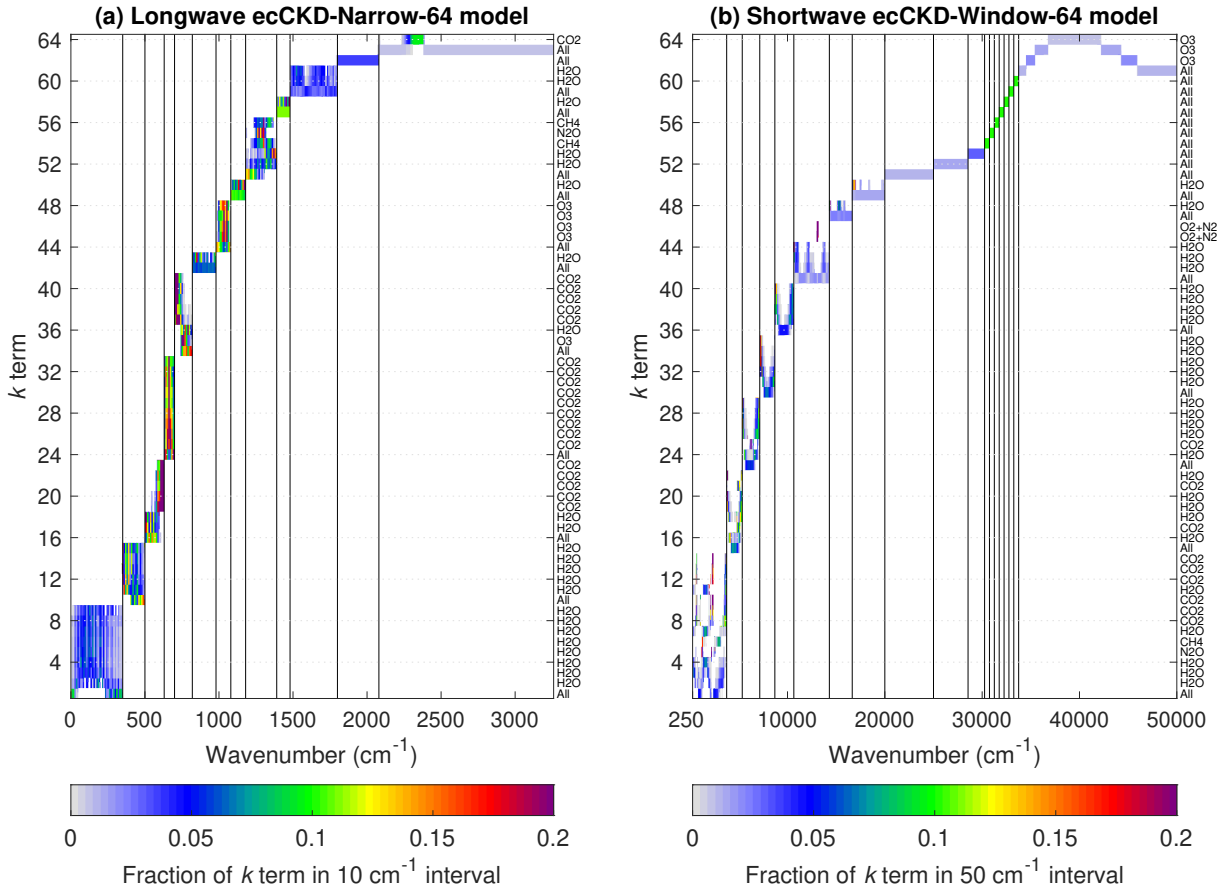

Figure S6: As Fig. 4 but for two ecCKD models with a total of 64 k-terms that use (a) the longwave 'Narrow' band structure proposed by Hogan and Matricardi (2020), which is very similar to that used by RRTMG, and (b) the shortwave 'Window' band structure that includes bands aligned with most of the near-infrared windows, plus bands for the red, green and blue parts of the visible spectrum and seven fine bands in the 295-330 nm wavelength range for computing UV index.

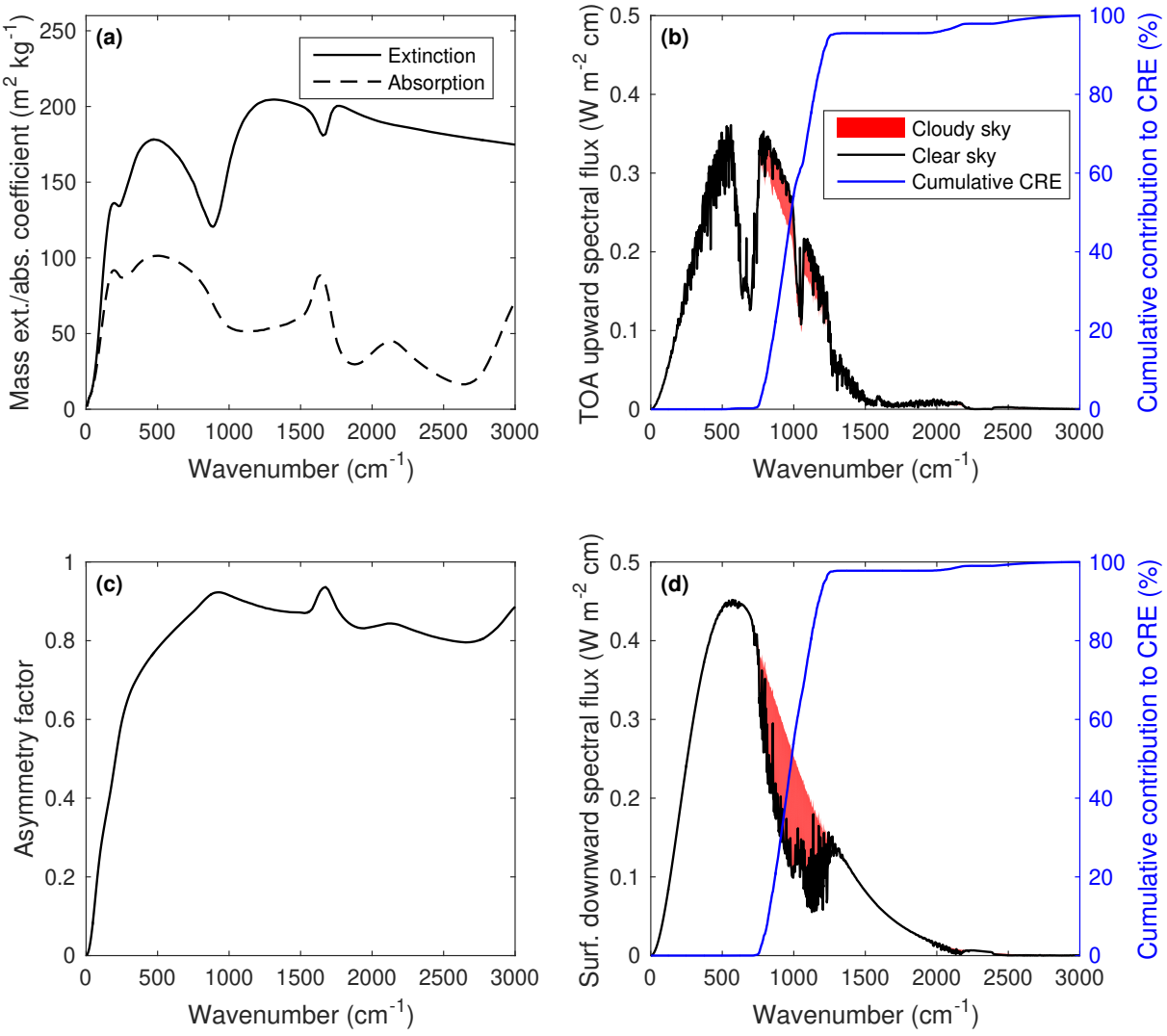

Figure S7: Supporting information for Fig. 10a–10c. (a) The longwave mass extinction and mass absorption coefficients of liquid clouds with an effective radius of 10 μm. (b) Line-by-line calculations of the upward spectral flux at top-of-atmosphere (TOA) for clear and cloudy skies (the latter for a very large liquid water path of 10 kg m^{-2}) considering the liquid cloud case described in Table 1, and (blue line) the cumulative spectral contribution to the cloud radiative effect for the same liquid water path. (c) As panel a but showing the cloud asymmetry factor. (d) As panel b but showing the downward spectral flux at the surface.

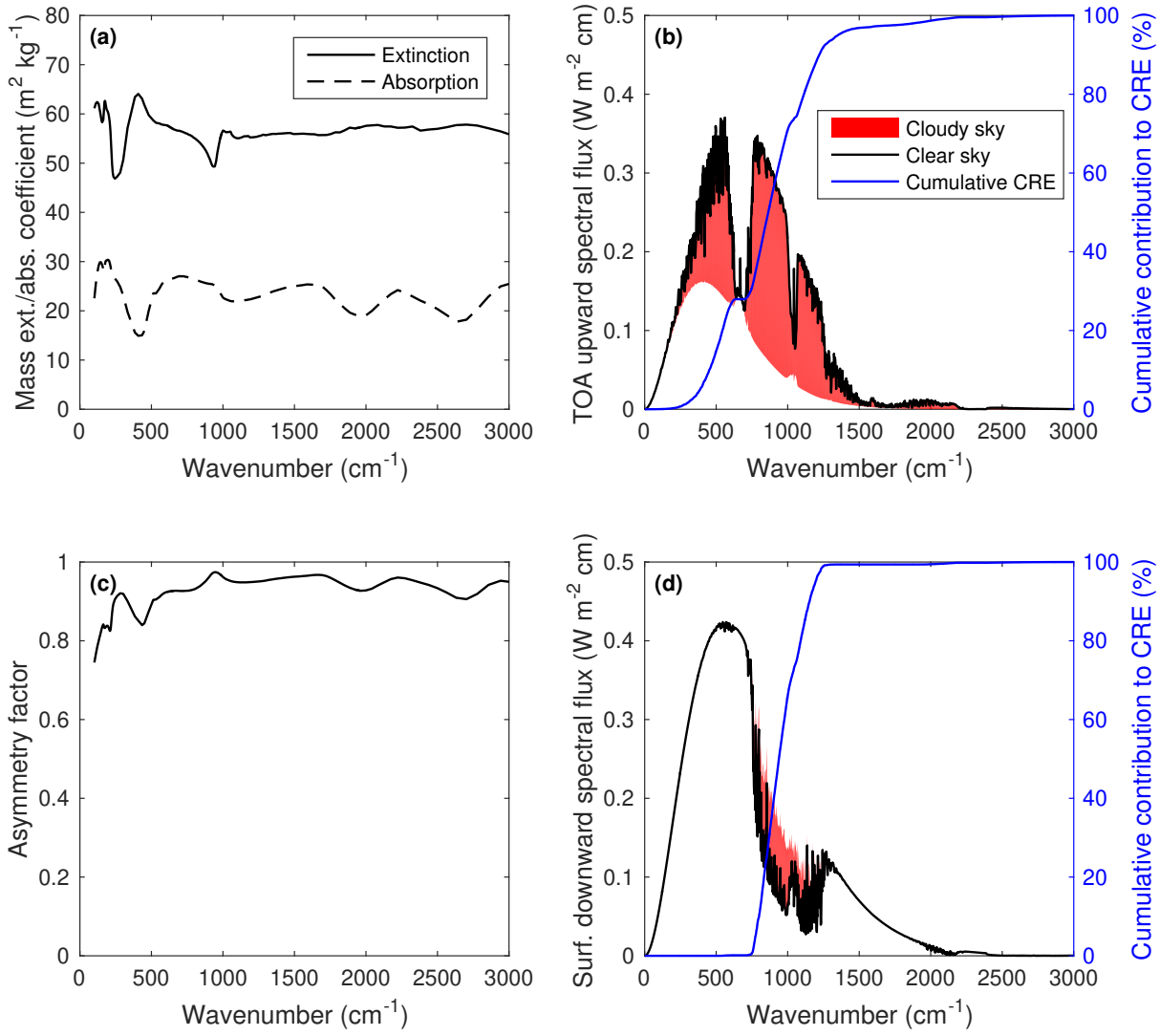

Figure S8: Supporting information for Fig. 11a–11c. (a) The longwave mass extinction and mass absorption coefficients of ice clouds with an effective radius of 30 μm. (b) Line-by-line calculations of the upward spectral flux at top-of-atmosphere (TOA) for clear and cloudy skies (the latter up to a very large ice water path of 10 kg m^{-2}) considering the ice cloud case described in Table 1, and (blue line) the cumulative spectral contribution to the cloud radiative effect for the same ice water path. (c) As panel a but showing the cloud asymmetry factor. (d) As panel b but showing the downward spectral flux at the surface.

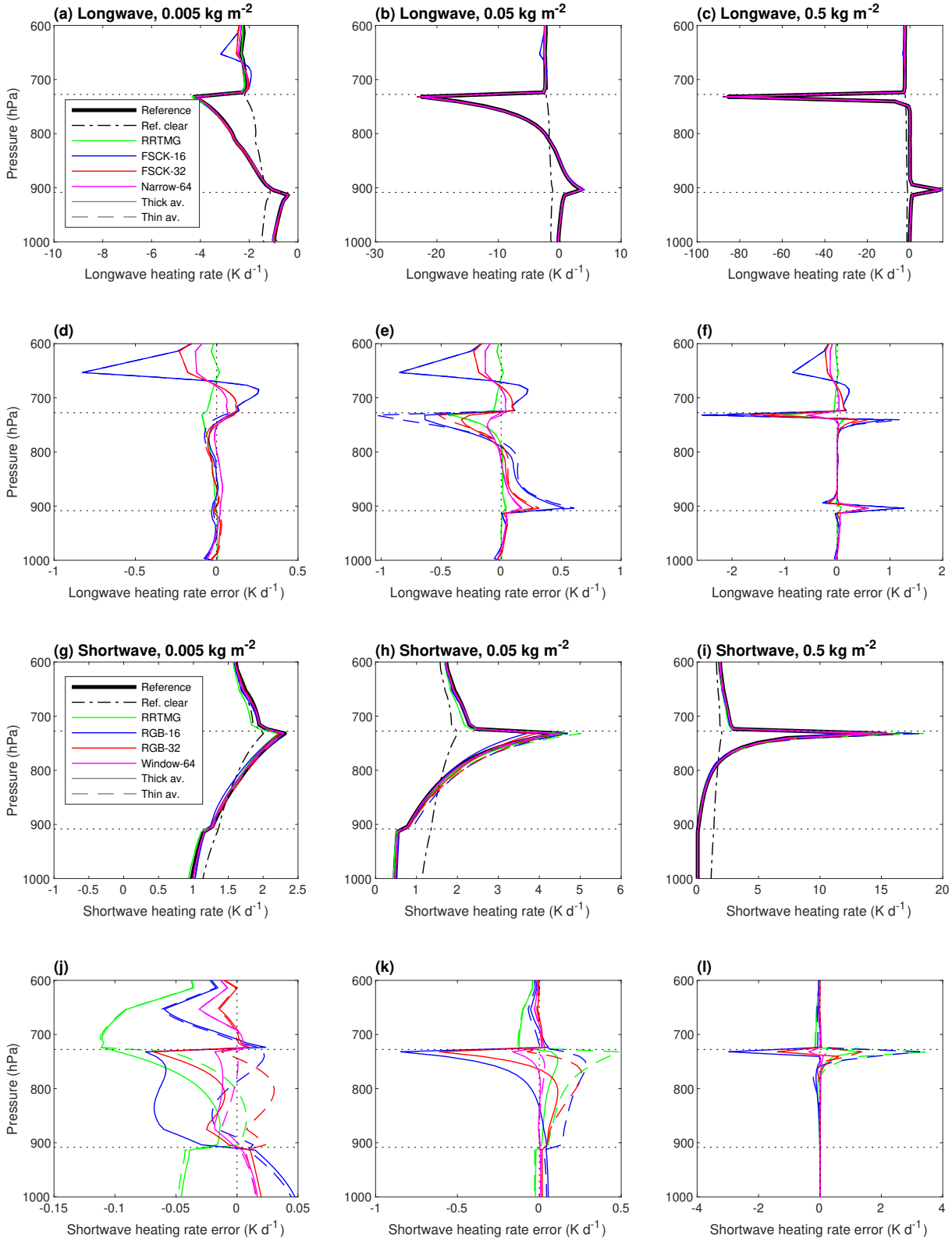

Figure S9: (a–c) Longwave heating-rate profiles for the liquid cloud case described in section 4 for three values of liquid water path given at the top of each panel, inluding the reference-line-by-line calculations, the same but for clear-sky, and four CKD models: RRTMG, ecCKD-FSCK-16, ecCKD-FSCK-32 and ecCKD-Narrow-64. The CKD models are run with both thick averaging (solid lines) and thin averaging (dashed lines). (d–f) For better visualization of the differences, these panels show the same as a–c but the difference between the CKD models and the reference calculations. (g–i) As panels a–f but for shortwave heating rates for a solar zenith angle of 60°C where the ecCKD models are ecCKD-RGB-16, ecCKD-RGB-32 and ecCKD-Window-64.

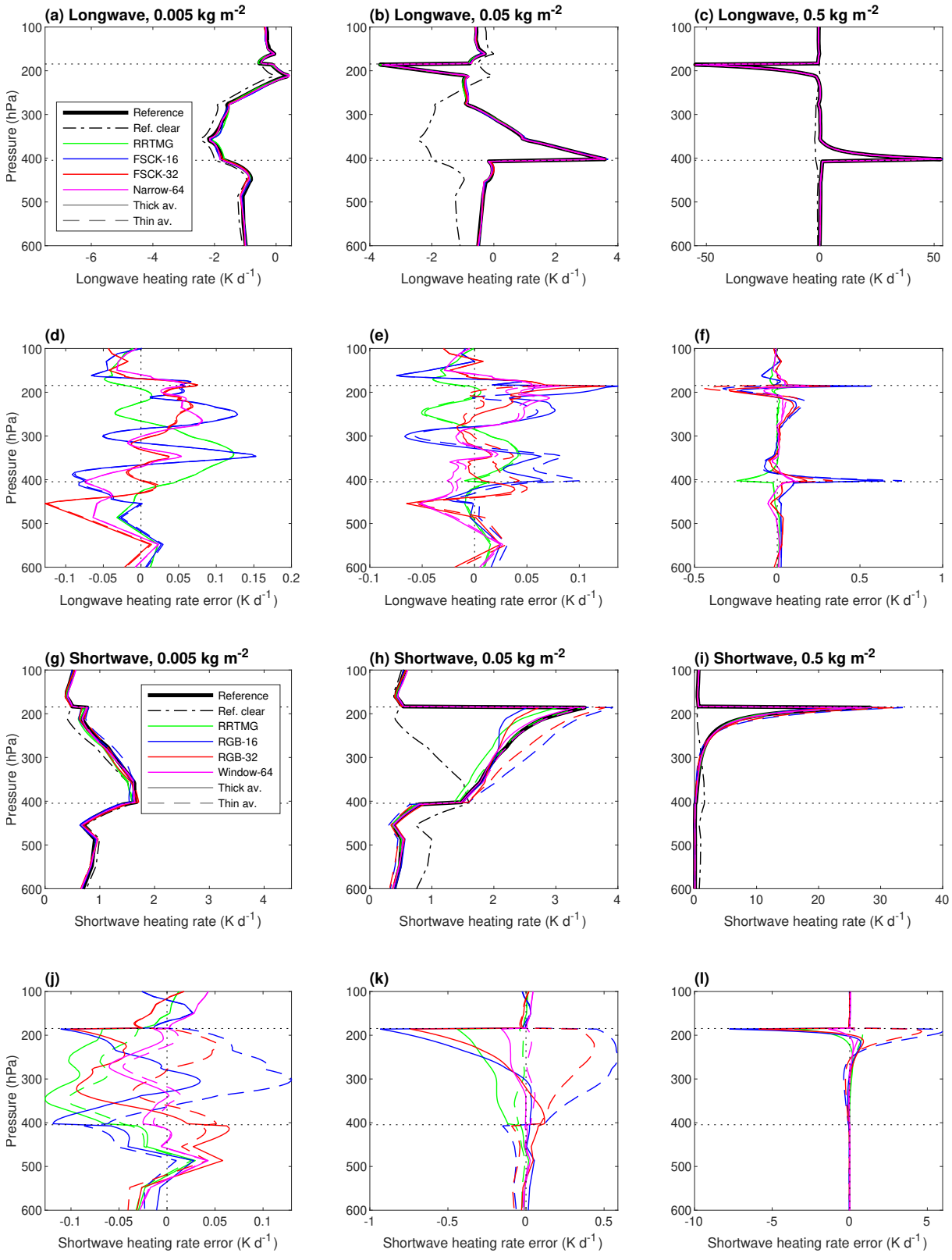

Figure S10: As Fig. S9 but for the ice cloud case described in section 4.